Nuclear Science and Techniques (2025) 36:67
https://doi.org/10.1007/s41365-024-01628-6

Beam test results of the prototype of the multi wire drift chamber for the CSR external-target experiment

Zhi Qin[1] · Zhou-Bo He[2] · Zhe Cao[3] · Tao Chen[3] · Zhi Deng[4] · Li-Min Duan[2,5] · Dong Guo[1] · Rong-Jiang Hu[2,5] · Jie Kong[2,5] · Can-Wen Liu[4] · Peng Ma[2,5] · Tian-Lei Pu[2,5] · Yi Qian[2,5] · Xiang-Lun Wei[2,5] · Shi-Hai Wen[2,5] · Xiang-Jie Wen[2,5] · Jun-Wei Yan[2,5] · He-Run Yang[2,5] · Zuo-Qiao Yang[2,5] · Yu-Hong Yu[2,5] · Zhi-Gang Xiao[1]

Received: 21 May 2024 / Revised: 20 September 2024 / Accepted: 27 September 2024 / Published online: 25 February 2025

Abstract
A half-size prototype of the multi wire drift chamber for the cooling storage ring external-target experiment (CEE) was assembled and tested in the 350 MeV/u Kr + Fe reactions at the heavy-ion research facility in Lanzhou. The prototype consists of six sense layers, where the sense wires are stretched in three directions X, U, and V; meeting 0°, 30°, and −30°, respectively, with respect to the vertical axis. The sensitive area of the prototype is 76 cm × 76 cm. The amplified and shaped signals from the anode wires were digitized in a serial capacity array. When operating at a high voltage of 1500 V on the anode wires, the efficiency for each layer is greater than 95%. The tracking residual is approximately 301 ± 2 μm. This performance satisfies the requirements of CEE.

Keywords Multi wire drift chamber (MWDC) · CSR external-target experiment (CEE) · Tracking

1 Introduction

Heavy ion collisions (HICs) in the beam energy region from hundreds of MeV/u to few GeV/u create nuclear matter with the density up to of a few times of saturation density ρ_0 [1–6]. Consequently, researchers can study the nuclear matter equation of state (nEOS) collision dynamics and QCD phase structure through observables identified from HICs, including direct flow, elliptic flow, triangle flow, meson production, and correlation functions, among others [7–13]. Owing to the operation of various experimental devices, including KAOS, FOPI, HADES, and SπRIT as an incomplete list, significant progress has been made in the constraint of nEOS in recent decades [14–19].

The most uncertain part of the nEOS thus far is the isovector sector, namely, the density dependence of the nuclear symmetry energy $E_{\rm sym}(\rho)$, particularly above ρ_0, where ρ_0 is the saturation density. Significant progress has been made in the last decade in constraining the density behavior of $E_{\rm sym}(\rho)$ near ρ_0 by applying various experimental probes, including π^-/π^+ yield and neutron-to-proton differential flow, in comparison with the prediction of transport

Zhi Qin and Zhou-Bo He have contributed equally to this work.

This work was supported by the National Natural Science Foundation of China (Nos. 11927901, 11875301, 11875302, U1867214, U1832105, U1832167), the Strategic Priority Research Program of Chinese Academy of Sciences (No. XDB34000000), the National Key R&D Program of China (No. 2018YFE0205200), the CAS "Light of West China" Program, and the Tsinghua University Initiative Scientific Research Program.

✉ Zhi Qin
qinz18@mails.tsinghua.edu.cn

Zhou-Bo He
hezhoubo@impcas.ac.cn

Zhi-Gang Xiao
xiaozg@tsinghua.edu.cn

[1] Department of Physics, Tsinghua University, Beijing 100084, China

[2] Institute of Modern Physics, Chinese Academy of Sciences, Lanzhou 730000, China

[3] University of Science and Technology of China, Hefei 230026, China

[4] Department of Engineering Physics, Tsinghua University, Beijing 100084, China

[5] School of Nuclear Science and Technology, University of Chinese Academy of Sciences, Beijing 100049, China

model calculations [20–25]. Despite the progress made, because of the complicated features of the production and transport of mesons and light nuclei in HICs, studies on the precise modeling of HIC and extraction of $E_{\rm sym}(\rho)$ are still ongoing, known as the transport model evaluation project (TMEP) [26–28]. The experimental efforts are ongoing. By combining the observation of the gravitational wave from the neutron star merging event GW170817 [29, 30] with nuclear physics data from terrestrial laboratories, the constraint becomes more convergent [31–33]. However, significant uncertainties remain and several questions are unanswered. For example, the convolution of the clustering and transport of the isospin degree of freedom [34, 35], along with the inconsistency between the neutron skin thickness of ^{208}Pb and ^{48}Ca [36–40]. The constraint of $E_{\rm sym}(\rho)$ becomes unprecedentedly more important than ever since the observation of GW170817. For the recent review, see Refs. [41–43].

Because of the long-standing interest and significance of studies on the nEOS, some new facilities providing heavy-ion beams from several hundreds of MeV/u to a few GeV/u have been constructed or proposed worldwide, such as CBM at FAIR, MPD at NICA, and LAMPS at RAON [44–46]. The cooling storage ring (CSR) at the heavy-ion facility in Lanzhou (HIRFL) is an accelerator complex that provides beams of all stable ion species with maximum energies of 2.8 GeV/u for protons and 0.5 GeV/u for uranium [47]. If equipped with an advanced experimental device, the HIRFL-CSR can provide novel opportunities for studies on various topics, including the properties of nuclear matter. For instance, one can revisit the π^-/π^+ yield ratio t/^{3}He in HICs at beam energies of hundreds of MeV/u [4, 48]. Additionally, using the proton-induced collisions on heavy targets at 2.8 GeV incident energy, the strangeness baryon Λ can be created. Hence, one can investigate the p-Λ interactions in cold nuclear matter at normal density via correlation functions, which have been widely applied to investigate the spatial time distribution of collisions and particle interactions [49–52].

After a decade of research and development (R&D), a CSR external-target experiment (CEE) is currently in construction [53–55]. It can measure lightly charged particles (LCPs) over almost the entire 4π solid angle in the center-of-mass frame. Figure 1 presents the schematic view of the CEE experiment. The main component of the CEE is a large-gap magnetic dipole that houses the tracking detectors. For mid-rapidity, the LCPs were tracked using two time projection chambers (TPCs) placed side-by-side, with an empty space in the middle for the beam to pass through. An inner time-of-flight (iTOF) wall was mounted on the left, right, and bottom sides of the TPCs to measure the TOF information of the tracks at mid-rapidity. For the large-rapidity region, an array consisting of three multi wire drift chambers (MWDCs) followed by an external TOF wall (eTOF) was designed to measure the LCPs. Both eTOF and iTOF

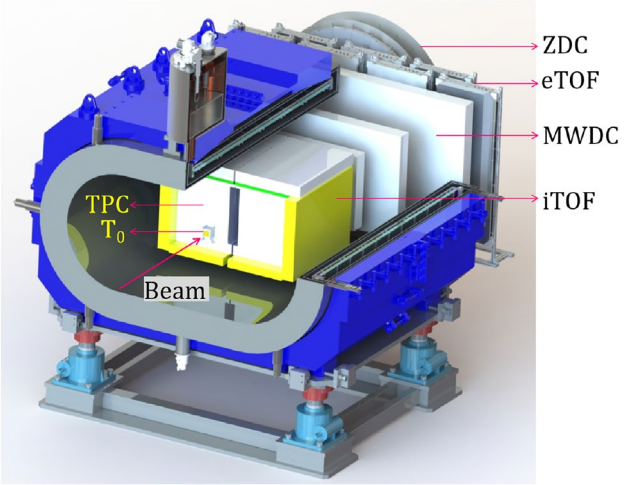

Fig. 1 (Color online) The technique design of the CSR external-target experiment (CEE). Details of AC and BM are not shown

are made of multilayer resistance plate counters (MRPC), requiring a time resolution of approximately 60 and 50 ps, respectively. A zero-degree counter (ZDC) was mounted on the downstream side to determine the reaction plane and provide complementary information to derive the centrality. The other sub-detectors, including the start time detector T_0, active collimator (AC), and silicon pixel beam spot monitor (BM) are mounted on the upstream side of the target on the beam line. According to the conceptual design of the CEE, the tracking residue of the MWDC array must be 300 μm and the momentum resolution must be 5%. The maximum event rate was 10^4 Hz, which corresponds to the 10^6 pps beam intensity when a 1% target was mounted [54].

From the start of the CEE project, extensive R&D have been conducted. All sub-detectors have progressed beyond the design stage. Currently, all CEE prototypes have been tested using cosmic rays and ion beams and have entered the engineering verification stage [48, 57–66]. Particularly for MWDC, the design, manufacturing, assembly, and source tests are presented in [66]. In this study, we focus on the beam test results of the MWDC prototype and demonstrate that its performance satisfies the requirements of the CEE design [54]. The remainder of this paper is organized as follows: Sect. 2 present the experimental setup for the beam test. The results and discussion are presented in Sect. 3. Section 4 provides the conclusions.

2 Experimental setup of the beam test

The beam test experiment was performed at the site where the CEE will be located in the HIRFL-CSR. The 350-MeV/u Kr beam was delivered by the main ring of the CSR, hitting an iron target with a thickness of approximately 1 mm.

Figure 2 presents the schematic view (a) and a real photograph (b) of the detector setup in the beam test. The prototypes of the sub-detectors were installed at approximately 20° with respect to the beam direction. Behind the target is the start-timing detector T_0, followed by two iTOF MRPCs (iTOF1 and iTOF2), and two eTOF MRPCs (eTOF1 and eTOF2). Subsequently, a full-sized TPC prototype was developed. The MWDC, sandwiched between two scintillators SC1 and SC2, was placed approximately 20 cm behind the TPC. On the farthest downstream from the setup, is the prototype of ZDC.

The half-sized prototype of the MWDC had the same structure as that of the real MWDC to be mounted on the CEE. However, the sensitive area of the prototype was 76 cm × 76 cm, which was smaller than the actual area. The prototype consists of six sense wire layers that are stretched in three directions, namely, *X*, *U*, and *V*, meeting 0°, 30°, and −30°, respectively, with respect to the vertical axis, as shown in Fig. 3(a). The size of each drift cell was 10 mm × 10 mm, i.e., the inter sense wire distance is 10 mm. As an example, Fig. 3(b) presents schematically the wire distributions of two neighboring drift cells of the *X* sense plane, from the transverse cross section point of view. In each direction, the two parallel sense planes are displaced by a half cell to remove the left-right ambiguity when a track passes through. The high voltage (HV) fed to the sense wire was 1500 V, and the working gas was a mixture of 80% argon and 20% CO_2 slightly beyond atmospheric pressure. Under this working condition, the energy resolution is about 22% for 5.9 keV X-rays in ^{55}Fe source test [66].

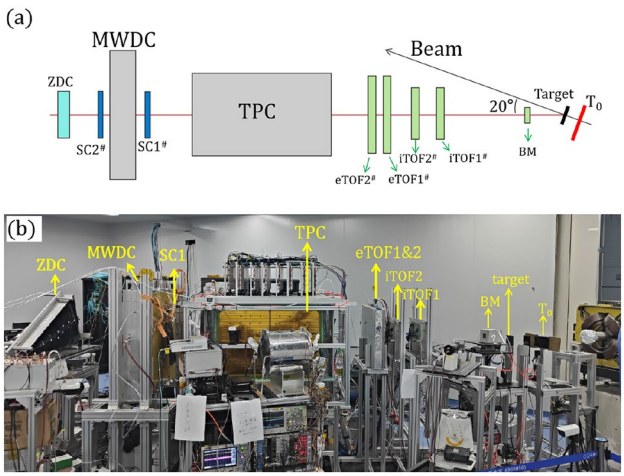

Fig. 2 (Color online) The detector setup in the test beam experiment performed at the CEE location on HIRFL-CSR. (**a**) A schematic view, (**b**) a real photograph

Owing to the large area of the MWDC in the CEE, to maintain the rigidity and precision of the wire distance, the frame of the large-area wire plane should be very thick and wider if using the conventional manufacturing technique. However, because the MWDC is placed in a dipole magnet with limited space, the dead area caused by the frame must be reduced. Thus, a new technique was developed to fabricate the wire plane. The wires stretched in advance on the rigid frame, made of aluminum alloy with carbon fibers were transferred to separate PCB boards attached to various duralumin ladders, which were mounted on the entire duralumin supporting frame. Each PCB covers only a partial area of the wire in each plane. Accurate wire spacing is further maintained by applying a fine-machined saw tooth, maintaining a wire spacing precision better than 20 μm. For details on the hardware manufacturing, refer to Ref. [66].

The signals from the sense wire are amplified and shaped by front-end electronics (FEE) that are mounted on PCB boards with each board housing 32 channels. The FEE signals are then sent to a serial capacity array (SCA) for digitization [67–69], where the pulses are sampled at a frequency of 80MHz followed by analog to digit conversion. Each SCA

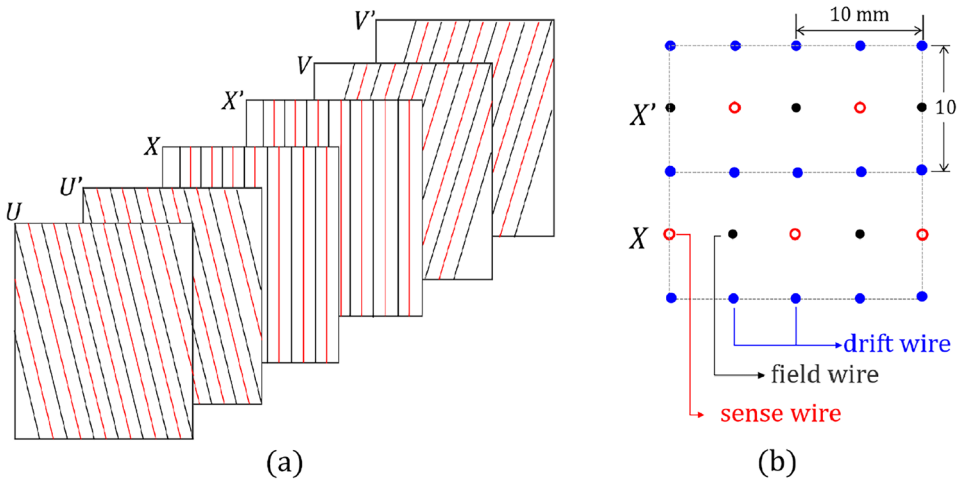

Fig. 3 (Color online) (**a**) The schematic view of the sense wire orientation. (**b**) The cross section view of the drift cells along X sense wires

board houses 16 channels, and six SCA boards are grouped into one back-end data module (BDM), which reads the data from the SCA and sends them to the main data acquisition (DAQ) system if a global trigger signal arrives. In the beam test, 192 channels of the MWDC prototype were connected, corresponding to 32 wires that were read out on each sense wire plane. Figure 4 presents the electronics scheme and the signal flow of the MWDC prototype.

The trigger system was built using field-programmable gate array (FPGA) technology. The signals from the iTOF and eTOF detectors were collected by the FEE boards to calculate the multiplicity, which was fed into the main trigger module (MTM) via optical fiber connections. If the trigger condition is satisfied, the MTM generates a trigger signal and sends it to all sub-detectors via the downlink chains. In the beam test, our trigger condition required the coincidence of T_0, iTOF, and eTOF. For the detailed construction of the FPGA-based trigger system, refer to Ref. [65].

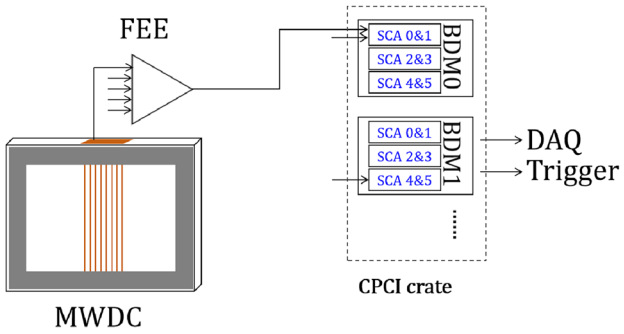

Fig. 4 (Color online) The schematic view of the electronics and the signal flow of the MWDC prototype

3 Results and discussion

In this section, we present the performance of the MWDC prototype in a beam test experiment.

Figure 5 presents a typical event display, where one can find 6 wires being fired by an incident particle. The last two panels with green fits denote the signals of the two scintillators SC1 and SC2. The abscissa represents the sampling time in ns. The bin width was 12.5 ns because the waveform was recorded at a sampling rate of 80 MHz. The ordinate indicates the signal amplitude. The signal shape was smooth, with a rising time of 100 ns and a descent time of 200 ns. Second, as shown in the figure, the baseline was stable in each channel. The fluctuation in the baseline for a single channel was approximately 25 channels, corresponding to 8 mV, according to our calibration.

Once a signal is identified for an individual channel, the asymmetric Gaussian function is used to fit the signal, and the amplitude is the direct fitting parameter. Figure 6(a) presents the distribution of the signal amplitude from the fired wires. As expected, the distribution exhibited an approximate Landau distribution. The most probable value of the amplitude situates at approximately channel number 200, corresponding to approximately 70 mV. Assuming that the incident particles are mainly protons with an average kinetic energy of 200 MeV, the most probable energy loss is estimated to be approximately 5.4 keV. The energy deposit of the minimum ionization particles is on average 2 keV and

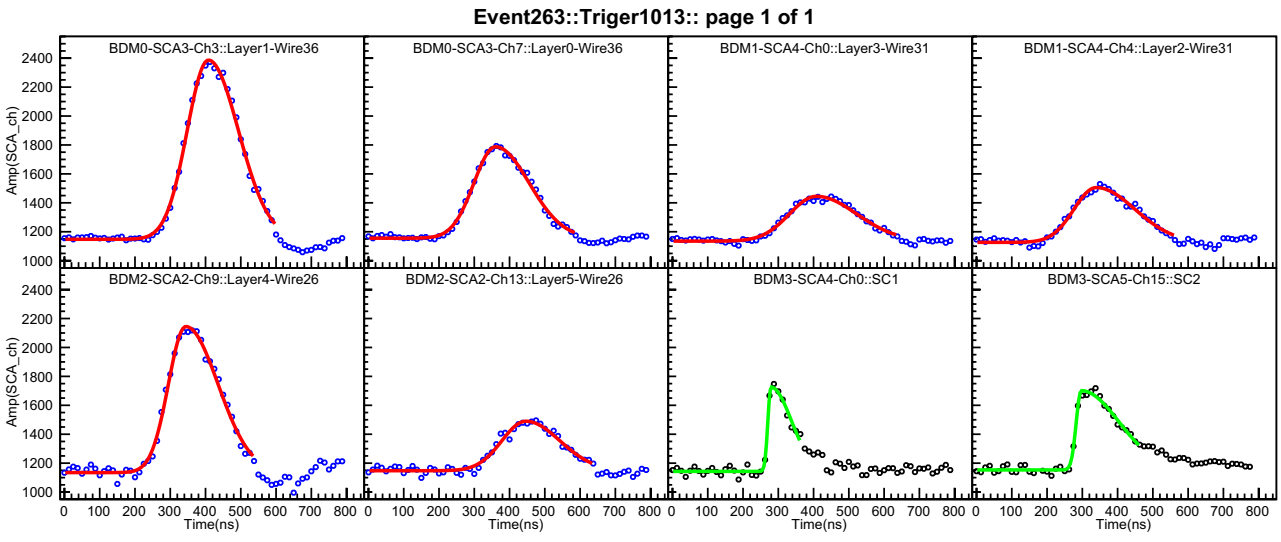

Fig. 5 (Color online) An event display with 6 wires fired. The last two panels in the lower row present the signals from SC1 and SC2, respectively. The pulses are fitted using asymmetric Gaussian function

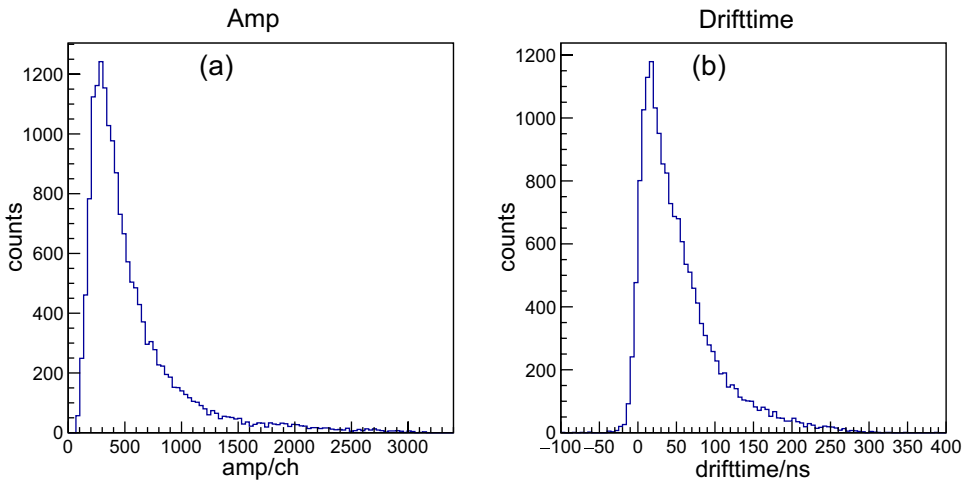

Fig. 6 (Color online) The distribution of the energy loss (**a**) and drift time with respect to the timing provided by SC1 and SC2 (**b**)

is expected to be situated in the vicinity of 25 mV, which is beyond the baseline fluctuation.

The Asymmetric Gaussian function provides the rising and falling edges of the signal waveform, and the timing information is extracted using the constant fraction discriminator algorithm with a constant fraction of 0.1. Meanwhile, one can also obtain the time of the two scintillators recorded by SCA using the same algorithm with a constant fraction of 0.5. The drift time is derived from the time difference between the wire and scintillator signals by considering the variation in the start time of the self-trigger sampling window in different SCA boards. Figure 6(b) presents the distribution of the drift time for the fired wires with respect to the timing provided by SC1 and SC2. Except for the main peak with a width of approximately 100 ns, there is also a long tail corresponding to the signal originating from the corners of the drift cell. The main peak rises rapidly, indicating a good zero drift time determination.

The histogram in Fig. 7(a) presents the count distribution of all the six layers for the events triggered by the coincidence of the two scintillators SC1 and SC2. For layers 2 and 5, the counts were slightly low because there was one dead channel in each of these two layers. The efficiency of the six layers is represented by solid dots on the right ordinate. The efficiency was 95% for layers 2 and 5 and 98% for the others. The efficiency of each individual layer is derived by counting the firing (0 or 1) on the wires in the vicinity of the crossing point of the track, which is recognized in the remaining five layers. Panel (b) shows the multiplicity distributions of the fired layers. Clearly, most events fire even layers. This is expected, because the fired wires in a given direction in X, U, and V typically come together in pairs. Because the coverage of the connected wires is slightly smaller than the area of the scintillators in front of and behind the MWDC prototype, the number of tracks registered by the scintillators misses the connected wires , causing the multiplicity to be distributed partly at 2 and 4.

Before demonstrating the tracking performance of the MWDC prototype, we investigated R-T calibration, where R and T are the drift distance and drift time, respectively. Calibration is performed using an iterative scheme. The

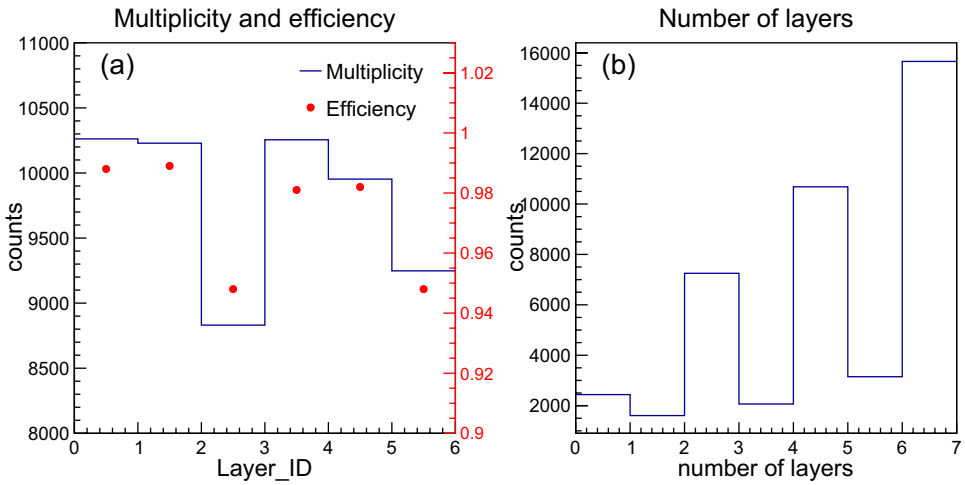

Fig. 7 (Color online) (**a**) The efficiency of each layer at 1500 V working voltage. (**b**) The distribution of the multiplicity of the fired layers

curve calculated from the Garfield++ code [70] was adopted as the initial *R*-*T* curve, as shown by the dashed curve in Fig. 8. With this initial condition, the tracks were fitted and the tracking residue was calculated as a function of the drift distance *R*. Once the tracking residual was obtained, it was used to correct the drift distance, and the fit is then redone. After several iterations, the *R*-*T* curve converges. The solid curve represents the calibrated *R*-*T* curve. The curve shows that the drift velocity in the middle of the drift cell is approximately $v_d \approx 4.5\,\mathrm{cm}/\mu\mathrm{s}$. The color palette presents the *R*-*T* distribution for all events. The width of this distribution contains information on the tracking residue δ_R, which is defined as the difference between the measured drift distance *R* obtained from the drift time and R–T curve and the expected drift distance R_{exp} after tracking, that is, $\delta_R = R - R_{exp}$, as depicted in the inset of Fig. 8.

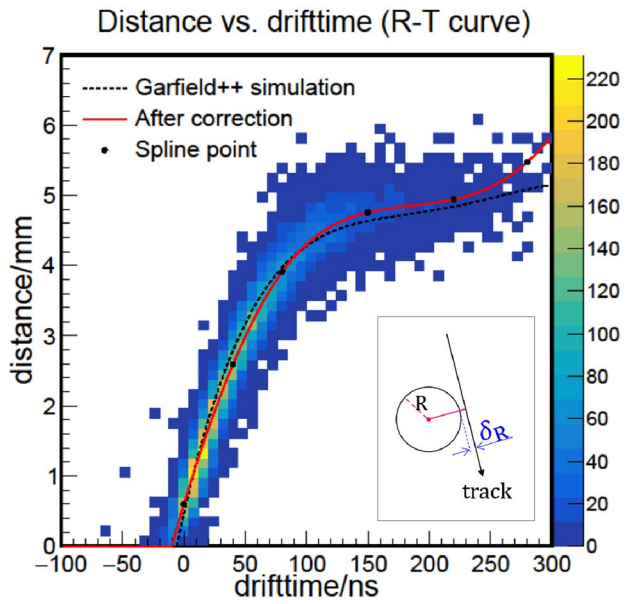

Fig. 8 (Color online) The *R*–*T* curve calibration. The inset shows the definition of the tracking residue δ_R

Figure 9(a) presents the tracking residue distribution. Here, we only counted the tracks firing six layers of the sense wire planes. The distribution exhibits a Gaussian shape. Using a Gaussian fit, the residue was derived $\sigma_t = 301 \pm 2\,\mu$m. This result is consistent with our result for an 10 cm × 10 cm prototype tested using cosmic-ray muons [53]. This suggests that the tracking performance did not deteriorate when the sensitive area increased. The tracking residue is consistent with the expected performance of the CEE MWDC array, which is 300 μm in the design [54]. By defining the beam direction as the *Z*-axis and the vertical direction as the *Y*-axis in the laboratory, one can get the azimuth angle ϕ and polar angle θ distributions for the tracks measured by the MWDC prototype are shown in panels (b) and (c), respectively. The peaks of θ and ϕ are situated at $\langle\theta\rangle = 20^\circ$ and $\langle\phi\rangle = 180^\circ$, indicating that the tracks originate from the target position, as expected.

The final problem remains to be solved for the application of MWDC to CEE. In a real beam experiment, the unreacted beam particles, which are the majority, pass through the MWDC array and cause serious saturation problem to the entire system. To treat malfunctions arising from the unreacted beam, we designed a deactivated area for each MWDC. Figure 10 presents an engineering prototype of the MWDC that was recently assembled and has the same size as the real MWDC1 to be mounted on the CEE. A stack of hollow rectangular PCBs, each corresponding to a layer of the wire frame, was mounted at the center of the MWDC. The wires in the vicinity of the beam line are soldered to the PCB as a bridge circumventing the beam path instead of passing through the entire area. The size of the deactivated

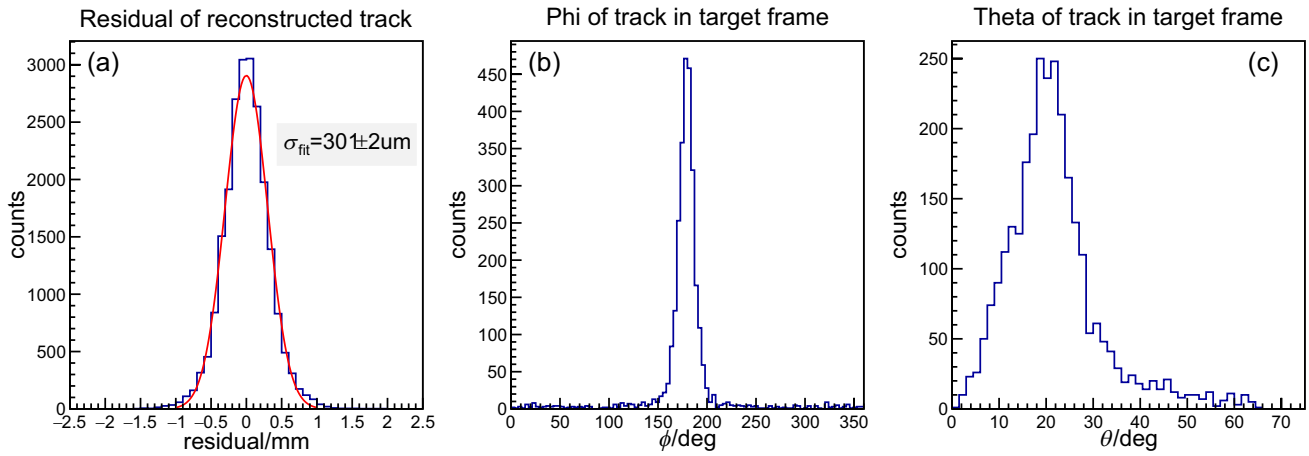

Fig. 9 (Color online) The distribution of the tracking residue. The curve is the fitting using Gaussian function

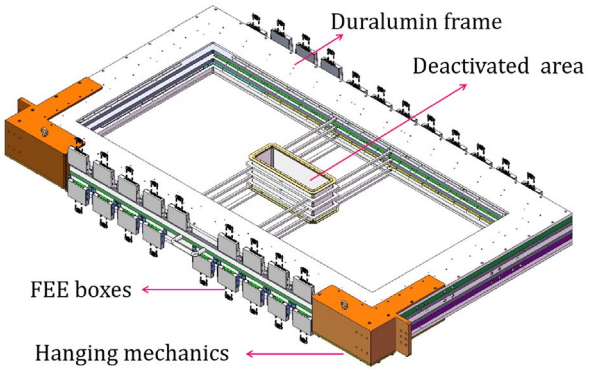

Fig. 10 (Color online) The mechanic structure of the MWDC. In the center is the inactive area, through which the unreacted beam particles pass through. The sensitive area of the detector is 136 cm (x) ×63 cm (y) and the deactivated area is 30 cm(x)×10 cm (y)

area was approximately 30 cm (x) × 10 cm (y) for the nearest MWDC (MWDC1) and 60 cm (x) × 20 cm (y) for the furthest MWDC (MWDC3) relative to the target. To verify the design, we performed a new beam test experiment in which the engineering prototype MWDC was placed on a beamline. At a beam intensity of 2×10^6 pps, which is greater than the usual condition for future experiments, the rate of signals with large amplitudes on the MWDC was much less than 10^{-3} of the beam intensity. Additionally, these low-rate signals, mainly induced by the projectile-like products of the interaction between the beam and upstream material on the path, cause no operational problems. The simulation-based transport model and Geant 4 packages suggest that the introduction of the deactivated area causes an insignificant loss of production because the inefficiency is only visible below 3° in the laboratory [48].

It was also verified that the introduction of the deactivated area did not influence the energy resolution of the prototype detector. As an example, Fig. 11 presents the energy spectra of the X-ray of the ^{55}Fe source recorded in two neighboring wires from the engineering prototype. The electronic setup is the same as that shown in Fig. 4. The results showed that the energy resolution was approximately 22%, in accordance with the prototype without the deactivated area [66]. The tracking performance of the MWDC prototype of the CEE was comparable to that of the CLAS experiment, in which a resolution of $310 - 395\ \mu$m was reported for the middle portion of the cell [71]. This result is also comparable to the MWDC of the same type operated at the ETF on the RIBLL-II, where 230 μm spatial resolution was achieved for 311 MeV/u ^{40}Ar beam particles [72]. The results of the beam and source tests demonstrate that the prototype of the MWDC, together with the electronics, can meet the requirements of the CEE experiment.

4 Conclusion

In conclusion, a prototype of the MWDC detector at CEE was assembled and operated in a beam test experiment of 350 MeV/u Kr + Fe. The prototypes of MWDC and all the other detectors, trigger systems, and DAQ systems were integrated in the beam test experiment. Being operated at working voltage of 1500 V, the MWDC worked correctly, with an average efficiency beyond 95% for all sense wire layers. The baseline fluctuation is approximately 7 mV. The $R - T$ curve was calibrated and a drift velocity of $v_{\mathrm{d}} \approx 4.5\ \mathrm{cm}/\mu\mathrm{s}$ was obtained. For events with $M_{\mathrm{layer}} = 6$, the tracking residue is approximately $301 \pm 2\ \mu$m. The energy resolution of the engineering prototype is typically 22% for ^{55}Fe X-rays, without being influenced by the introduction of a deactivated area in the center to avoid malfunction caused by unreacted beam particles. The experimental results demonstrate that the MWDC satisfied the requirements of the CEE experiment.

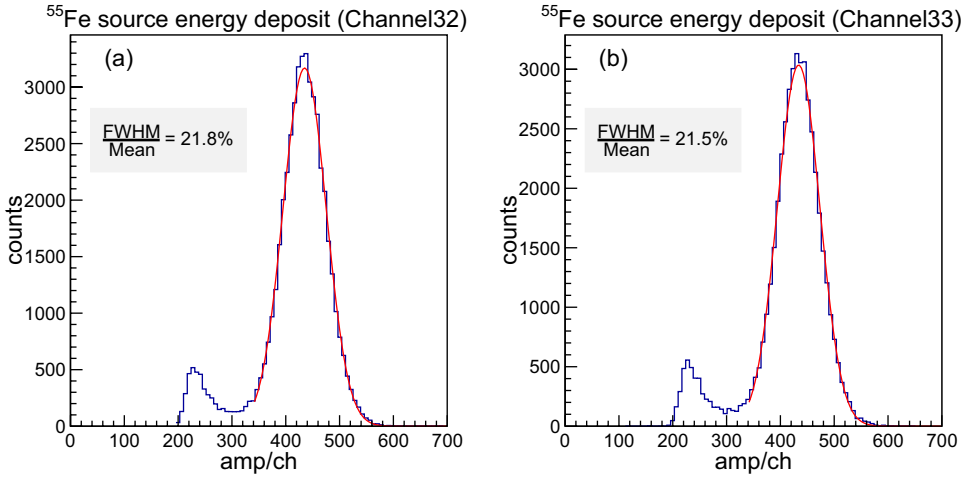

Fig. 11 (Color online) The energy spectra of the X-rays from the ^{55}Fe source in two channels for the engineering prototype are shown in Fig. 10. The operation HV here is 1400 V

Author Contributions All authors contributed to the study conception and design. Material preparation, data collection and analysis were performed by Zhi Qin, Zhou-Bo He, Tao Chen and Can-Wen Liu. The first draft of the manuscript was written by Zhi Qin and Zhi-Gang Xiao; all authors commented on previous versions of the manuscript. All authors read and approved the final manuscript.

Data Availability The data that support the findings of this study are openly available in Science Data Bank at https://cstr.cn/31253.11.sciencedb.j00186.00446 and https://doi.org/10.57760/sciencedb.j00186.00446.

Declarations

Conflict of interest The authors declare that they have no conflict of interest.

References

1. A. Sorensen, K. Agarwal, K.W. Brown et al., Dense nuclear matter equation of state from heavy-ion collisions. Prog. Part. Nucl. Phys. **134**, 104080 (2024). https://doi.org/10.1016/j.ppnp.2023.104080
2. W. Reisdorf, A. Andronic, A. Gobbi et al., Nuclear stopping from 0.09*A* to 1.93*A* GeV and its correlation to flow. Phys. Rev. Lett. **92**, 232301 (2004). https://doi.org/10.1103/PhysRevLett.92.232301
3. F. Fu, Z.G. Xiao, Y.P. Zhang et al., Nuclear stopping and compression in heavy-ion collisions at intermediate energies. Phys. Lett. B **666**, 359–363 (2008). https://doi.org/10.1016/j.physletb.2008.07.063
4. M. Zhang, Z.G. Xiao, B.A. Li et al., A systematic study of the pi-/pi+ ratio in heavy-ion collisions with the same neutron/proton ratio but different masses. Phys. Rev. C **80**, 034616 (2009). https://doi.org/10.1103/PhysRevC.80.034616
5. M.S. Abdallah, B.E. Aboona, J. Adam et al., Disappearance of partonic collectivity in $\sqrt{s_{\rm NN}}$ = 3 GeV Au+Au collisions at RHIC. Phys. Lett. B **827**, 137003 (2022). https://doi.org/10.1016/j.physletb.2022.137003
6. M.S. Abdallah, B.E. Aboona, J. Adam et al., Light nuclei collectivity from $\sqrt{s_{\rm NN}}$ = 3 GeV Au+Au collisions at RHIC. Phys. Lett. B **827**, 136941 (2022). https://doi.org/10.1016/j.physletb.2022.136941
7. B.A. Li, A. Ramos, G. Verde et al., Topical issue on nuclear symmetry energy. Eur. Phys. J. A **50**, 9 (2014). https://doi.org/10.1140/epja/i2014-14009-x
8. S.W. Lan, S.S. Shi, Anisotropic flow in high baryon density region. Nucl. Sci. Tech. **33**, 21 (2022). https://doi.org/10.1007/s41365-022-01006-0
9. L.G. Pang, X.N. Wang, Bayesian analysis of nuclear equation of state at high baryon density. Nucl. Sci. Tech. **34**, 194 (2023). https://doi.org/10.1007/s41365-023-01345-6
10. P.C. Li, Y.J. Wang, Q.F. Li et al., Transport model analysis of the pion interferometry in Au+Au collisions at $E_{\rm beam}$=1.23 GeV/nucleon. Sci. China Phys. Mech. Astron. **66**, 222011 (2023). https://doi.org/10.1007/s11433-022-2026-5
11. S. Pratt, Constraining the high density nuclear equation of state with femtoscopic pion correlations. Sci. China-Phys. Mech. Astron. **66**, 252032 (2023). https://doi.org/10.1007/s11433-023-2080-0
12. K.J. Sun, L.W. Chen, C.M. Ko et al., Light nuclei production and QCD phase transition in heavy-ion collisions. Nucl. Tech. (in Chinese) **46**, 040012 (2023). https://doi.org/10.11889/j.0253-3219.2023.hjs.46.040012
13. Y. Zhang, D.W. Zhang, X.F. Luo et al., Experimental study of the QCD phase diagram in relativistic heavy-ion collisions. Nucl. Tech. (in Chinese) **46**, 040001 (2023). https://doi.org/10.11889/j.0253-3219.2023.hjs.46.040001
14. W. Reisdorf, Y. Leifels, A. Andronic et al., Systematics of azimuthal asymmetries in heavy ion collisions in the 1 *A*GeV regime. Nucl. Phys. A **876**, 1–60 (2012). https://doi.org/10.1016/j.nuclphysa.2011.12.006
15. P. Danielewicz, R. Lacey, W.G. Lynch, Determination of the equation of state of dense matter. Science **298**, 1592–1596 (2002). https://doi.org/10.1126/science.1078070
16. C. Fuchs, A. Faessler, E. Zabrodin et al., Probing the nuclear equation of state by K+ production in heavy ion collisions. Phys. Rev. Lett. **86**, 1974–1977 (2001). https://doi.org/10.1103/PhysRevLett.86.1974
17. C.T. Sturm, I. Böttcher, M. Dębowski et al., Evidence for a soft nuclear equation of state from kaon production in heavy ion collisions. Phys. Rev. Lett. **86**, 39–42 (2001). https://doi.org/10.1103/PhysRevLett.86.39
18. C. Hartnack, H. Oeschler, J. Aichelin, Hadronic matter is soft. Phys. Rev. Lett. **96**, 012302 (2006). https://doi.org/10.1103/PhysRevLett.96.012302
19. J. Adamczewski-Musch et al., Directed, elliptic, and higher order flow harmonics of protons, deuterons, and tritons in Au+Au collisions at $\sqrt{s_{\rm NN}}$ = 2.4 GeV. Phys. Rev. Lett. **125**, 262301 (2020). https://doi.org/10.1103/PhysRevLett.125.262301
20. W. Reisdorf et al., Systematics of pion emission in heavy ion collisions in the 1 *A*GeV regime. Nucl. Phys. A **781**, 459–508 (2007). https://doi.org/10.1016/j.nuclphysa.2006.10.085
21. Z. Xiao, B.A. Li, L.W. Chen et al., Circumstantial evidence for a soft nuclear symmetry energy at suprasaturation densities. Phys. Rev. Lett. **102**, 062502 (2009). https://doi.org/10.1103/PhysRevLett.102.062502
22. Z.G. Xiao, G.C. Yong, L.W. Chen et al., Probing nuclear symmetry energy at high densities using pion, kaon, eta and photon productions in heavy-ion collisions. Eur. Phys. J. A **50**, 37 (2014). https://doi.org/10.1140/epja/i2014-14037-6
23. Y.J. Wang, Q.F. Li, Application of microscopic transport model in the study of nuclear equation of state from heavy ion collisions at intermediate energies. Front. Phys. **15**, 44302 (2020). https://doi.org/10.1007/s11467-020-0964-6
24. M.D. Cozma, Neutron-proton elliptic flow difference as a probe for the high density dependence of the symmetry energy. Phys. Lett. B **700**, 139–144 (2011). https://doi.org/10.1016/j.physletb.2011.05.002
25. J. Estee, W.G. Lynch, C.Y. Tsang et al., Probing the symmetry energy with the spectral pion ratio. Phys. Rev. Lett. **126**, 162701 (2021). https://doi.org/10.1103/PhysRevLett.126.162701
26. Y.X. Zhang, Y.J. Wang, M. Colonna et al., Comparison of heavy-ion transport simulations: collision integral in a box. Phys. Rev. C **97**, 034625 (2018). https://doi.org/10.1103/PhysRevC.97.034625
27. A. Ono, J. Xu, M. Colonna et al., Comparison of heavy-ion transport simulations: collision integral with pions and Δ resonances in a box. Phys. Rev. C **100**, 044617 (2019). https://doi.org/10.1103/PhysRevC.100.044617
28. M. Colonna, Y.X. Zhang, Y.J. Wang et al., Comparison of heavy-ion transport simulations: mean-field dynamics in a box. Phys. Rev. C **104**, 024603 (2021). https://doi.org/10.1103/PhysRevC.104.024603
29. B.P. Abbott, R. Abbott, T.D. Abbott et al., GW170817: Observation of gravitational waves from a binary neutron star inspiral. Phys. Rev. Lett. **119**, 161101 (2017). https://doi.org/10.1103/PhysRevLett.119.161101
30. B.P. Abbott, R. Abbott, T.D. Abbott et al., GW170817: Measurements of neutron star radii and equation of state. Phys. Rev.

Lett. **121**, 161101 (2018). https://doi.org/10.1103/PhysRevLett.121.161101
31. S. Huth, P.T.H. Pang, I. Tews et al., Constraining neutron-starmatter with microscopic and macroscopic collisions. Nature **606**, 276–280 (2022). https://doi.org/10.1038/s41586-022-04750-w
32. Y. Liu, Y. Wang, Y. Cui et al., Insights into the pion production mechanism and the symmetry energy at high density. Phys. Rev. C **103**, 014616 (2021). https://doi.org/10.1103/PhysRevC.103.014616
33. Y. Zhou, L.W. Chen, Z. Zhang, Equation of state of dense matter in the multimessenger era. Phys. Rev. D **99**, 121301 (2019). https://doi.org/10.1103/PhysRevD.99.121301
34. Y. Wang, F. Guan, Q. Wu et al., The emission order of hydrogen isotopes via correlation functions in 30 MeV/u Ar+Au reactions. Phys. Lett. B **825**, 136856 (2022). https://doi.org/10.1016/j.physletb.2021.136856
35. Y. Wang, F. Guan, X. Diao et al., Observing the ping-pong modality of the isospin degree of freedom in cluster emission from heavy-ion reactions. Phys. Rev. C **107**, L041601 (2023). https://doi.org/10.1103/PhysRevC.107.L041601
36. D. Adhikari Jung et al., Accurate determination of the neutron skin thickness of ^{208}Pb through parity-violation in electron scattering. Phys. Rev. Lett. **126**, 172502 (2021). https://doi.org/10.1103/PhysRevLett.126.172502
37. B.T. Reed, F.J. Fattoyev, C.J. Horowitz et al., Implications of PREX-2 on the equation of state of neutron-rich matter. Phys. Rev. Lett. **126**, 172503 (2021). https://doi.org/10.1103/PhysRevLett.126.172503
38. D. Adhikari, H. Albataineh, D. Androic et al., Precision determination of the neutral weak form factor of ^{48}Ca. Phys. Rev. Lett. **129**, 042501 (2022). https://doi.org/10.1103/PhysRevLett.129.042501
39. P.G. Reinhard, X. Roca-Maza, W. Nazarewicz, Combined theoretical analysis of the parity-violating asymmetry for ^{48}Ca and ^{208}Pb. Phys. Rev. Lett. **129**, 232501 (2022). https://doi.org/10.1103/PhysRevLett.129.232501
40. Z. Zhang, L.W. Chen, Bayesian inference of the symmetry energy and the neutron skin in ^{48}Ca and ^{208}Pb from CREX and PREX-2. Phys. Rev. C **108**, 024317 (2023). https://doi.org/10.1103/PhysRevC.108.024317
41. M. Colonna, Collision dynamics at medium and relativistic energies. Prog. Part. Nucl. Phys. **113**, 103775 (2020). https://doi.org/10.1016/j.ppnp.2020.103775
42. B.A. Li, B.J. Cai, W.J. Xie et al., Progress in constraining nuclear symmetry energy using neutron star observables since GW170817. University **7**, 182 (2021). https://doi.org/10.3390/universe7060182
43. L.W. Chen, X. Dong, K. Fukushima et al., Nuclear matter at high density and equation of state, in properties of QCD matter at high baryon density (eds) by X. Luo, Q. Wang, N. Xu, Springer, Singapore, 2022)
44. V. Friese, The CBM experiment at GSI/FAIR. Nucl. Phys. A **774**, 377–386 (2006). https://doi.org/10.1016/j.nuclphysa.2006.06.018
45. G. Musulmanbekov, NICA Collaboration, The NICA/MPD project at JINR. Nucl. Phys. A **862–863**, 244–250 (2011). https://doi.org/10.1016/j.nuclphysa.2011.05.047
46. B. Hong, D.S. Ahn, J.K. Ahn et al., Status of LAMPS at RAON. Nucl. Instr. Meth. B **541**, 260 (2023). https://doi.org/10.1016/j.nimb.2023.05.030
47. Y.J. Yuan, D.Q. Gao, L.Z. Ma et al., Present status of HIRFL complex in Lanzhou. J. Phys. Conf. Ser. **1401**, 012003 (2020). https://doi.org/10.1088/1742-6596/1401/1/012003
48. D. Guo, X. He, P. Li et al., Studies of nuclear equation of state with the HIRFL-CSR external-target experiment. Eur. Phys. J. A **60**, 36 (2024). https://doi.org/10.1140/epja/s10050-024-01245-2
49. S.E. Koonin, Proton pictures of high-energy nuclear collisions. Phys. Lett. B **70**, 43 (1977). https://doi.org/10.1016/0370-2693(77)90340-9
50. R. Lednicky, V.L. Lyuboshits, Final state interaction effect on pairing correlations between particles with small relative momenta. Sov. J. Nucl. Phys. **35**, 770 (1982)
51. M.A. Lisa, S. Pratt, R. Soltz et al., Femtoscopy in relativistic heavy ion collisions: two decades of progress. Annu. Rev. Nucl. Part. Sci. **55**, 357 (2005). https://doi.org/10.1146/annurev.nucl.55.090704.151533
52. G. Verde, A. Chbihi, R. Ghetti et al., Correlations and characterization of emitting sources. Eur. Phys. J. A **30**, 81–108 (2006). https://doi.org/10.1140/epja/i2006-10109-6
53. H. Yi, Z. Zhang, Z.G. Xiao et al., Prototype studies on the forward MWDC tracking array of the external target experiment at HIRFL-CSR. China Phys. C **38**, 126002 (2014). https://doi.org/10.1088/1674-1137/38/12/126002
54. L.M. Lyu, H. Yi, Z.G. Xiao et al., Conceptual design of the HIRFL-CSR external-target experiment. Sci. China Phys. Mech. Astron. **60**, 012021 (2017). https://doi.org/10.1007/s11433-016-0342-x
55. D. Hu, M. Shao, Y. Sun et al., A T0/Trigger detector for the external target experiment at CSR. JINST **12**, C06010 (2017). https://doi.org/10.1088/1748-0221/12/06/C06010
56. L.M. Lyu, H. Yi, L.M. Duan et al., Simulation and prototype testing of multi-wire drift chamber arrays for the CEE. Nucl. Sci. Tech. **31**, 11 (2020). https://doi.org/10.1007/s41365-019-0716-x
57. B. Wang, D. Han, Y. Wang et al., The CEE-eTOF wall constructed with new sealed MRPC. JINST **15**, C08022 (2020). https://doi.org/10.1088/1748-0221/15/08/C08022
58. B. Wang, H. Xu, X. Chen et al., The external time-of-flight wall for CEE experiment. Eur. Phys. J. C **83**, 817 (2023). https://doi.org/10.1140/epjc/s10052-023-11806-2
59. D. Hu, J. Lu, J. Zhou et al., Extensive beam test study of prototype MRPCs for the T0 detector at the CSR external-target experiment. Eur. Phys. J. C **80**, 282 (2020). https://doi.org/10.1016/j.jnucmat.2015.06.030
60. S.H. Zhu, H.B. Yang, H. Pei et al., Prototype design of readout electronics for zero degree calorimeter in the HIRFL-CSR external-target experiment. JINST **16**, P08014 (2021). https://doi.org/10.1088/1748-0221/16/08/P08014
61. X. Wang, D. Hu, M. Shao et al., CEE inner TOF prototype design and preliminary test results. JINST **17**, P09023 (2022). https://doi.org/10.1088/1748-0221/17/09/P09023
62. H.L. Wang, Z. Wang, C.S. Gao et al., Design and tests of the prototype a beam monitor of the CSR external target experiment. Nucl. Sci. Tech. **33**, 36 (2022). https://doi.org/10.1007/s41365-022-01021-1
63. J. Liu, C. Gao, H. Wang et al., Design and preliminary characterization of a novel silicon charge sensor for the gaseous beam monitor at the CSR external-target experiment. Nucl. Instrum. Meth. A **1047**, 167786 (2023). https://doi.org/10.1016/j.nima.2022.167786
64. L.K. Liu, H. Pei, Y.P. Wang et al., Event plane determination from the zero degree calorimeter at the cooling storage ring external-target experiment. Nucl. Sci. Tech. **34**, 100 (2023). https://doi.org/10.1007/s41365-023-01262-8
65. D. Guo, H. Xu, D. Qi et al., The trigger system for the HIRFL-CSR external-target experiment. JINST **19**, T02018 (2024). https://doi.org/10.1088/1748-0221/19/02/T02018
66. Z.B. He, Z. Qin, P. Ma et al., Development of a MWDC prototype of the CSR external-target experiment. Nucl. Sci. Tech. **35**, 174 (2024). https://doi.org/10.1007/s41365-024-01515-0
67. X.Y. Zhao, F. Liu, Z. Deng et al., GERO: a general SCA-based readout ASIC for micro-pattern gas detectors with configurable storage depth and on-chip digitizer. Nucl. Sci. Tech. **30**, 131 (2019). https://doi.org/10.1007/s41365-019-0659-2

68. J.P. Xu, C.W. Liu, T.L. Pu et al., Development of a multi-channel readout electronics verification system for MWDC detectors. Radiat. Detect. Technol. Methods **6**, 281 (2022). https://doi.org/10.1007/s41605-022-00347-z
69. F. Liu, Z. Deng, X.Y. Zhao et al., A switched capacitor waveform digitizing ASIC at cryogenic temperature for HPGe detectors. IEEE Trans. Nucl. Sci. **68**(8), 2315 (2021). https://doi.org/10.1109/TNS.2021.3095845
70. H. Schindler, R. Veenhof, R., Garfield++ simulation of ionisation based tracking detectors (2018). https://garfieldpp.web.cern.ch/garfieldpp/
71. M.D. Mestayer, K. Adhikari, R.P. Bennett et al., The CLAS12 drift chamber system. Nucl. Instrum. Meth. A **959**, 163518 (2020). https://doi.org/10.1016/j.nima.2020.163518
72. Y.Z. Sun, Z.Y. Sun, S.T. Wang et al., The drift chamber array at the external target facility in HIRFL-CSR. Nucl. Instrum. Meth. A **894**, 72–80 (2018). https://doi.org/10.1016/j.nima.2018.03.044